AERODYNAMIC ANALYSIS OF AN ELASTO-FLEXIBLE MORPHING WING CONFIGURATION

B. Béguin, Ch. Breitsamter, N. Adams
Institute of Aerodynamics and Fluid Mechanics, TU München
Boltzmannstr. 15, 85748 Garching, Germany

Overview

This paper concentrates on the aero-elastic investigation of a morphing wing concept using a compliant membrane as lifting surface to allow large variations of the planform geometry (aspect ratio and sweep angle). The results of force measurements performed on five different wing configurations shows that varying the planform effectively alters the lift and drag characteristics in such a way that relatively high lift-to-drag ratios can be maintained over a broader range of flow conditions. Due to its intrinsic construction, the wing surface passively deforms under aerodynamic loading resulting in a pronounced dependency of the aerodynamic characteristics on the flow conditions. To provide insight into the complex flow-structure interaction mechanisms involved, the deflection of the membrane of two different wing configurations is measured at various flow conditions (dynamic pressures and angles of attack) using a stereo photogrammetry technique. The results highlight the broad range of airfoil shapes the wing can take on, depending on the flow conditions and on the wing planform.

1. INTRODUCTION

1.1. Morphing aircrafts

In recent years, an increased amount of resources is spent for the development of aircrafts able to considerably alter their shape with the main goal to improve efficiency and to expand the flight envelope compared to conventional rigid configurations. In fact, the flight performance of an aircraft is directly related to its geometry and thus, in flight reconfiguration would allow a single aircraft to accomplish different mission roles efficiently and effectively. In current aircraft design, common form-variability solutions are, for example, the leading and trailing edge flaps to change the wing camber, or Fowler flaps to change the wing area in addition, typically used for additional lift capability at low speed (take off and landing). Variable sweep wings, used to address the conflict between subsonic and supersonic flight conditions, are other examples illustrating large scale geometry variation. However, these current technologies differ from what is nowadays commonly understood under “morphing” because they involve the movement of discrete parts, coming at the expense of increased weight and aerodynamic inefficiency due to discontinuities and gaps in the geometry. Rather, ”morphing” seeks the extension of these current solutions with new technologies to allow continuous shape changes in all planform geometry characteristics of seamless aerodynamic surfaces. Even if the benefits of morphing are obvious for the aerodynamicist, technical realisations are still a critical issue. In fact, the design of morphing aircraft addresses new challenges concerning the design methods, materials, actuators and flight control ([1], [2]). Moreover, morphing wings also come with additional weight and energy consumption, due to the addition of actuators and other materials used to physically morph the wing. In this context, Ref. [12] presents a detailed discussion about the question whether the improved aerodynamics created by wing morphing offsets the penalties associated with the additional weight and energy consumption to yield a more optimum system. It concludes that definite benefits can effectively be reached considering that the mission is not dominated by one aspect (such as cruise). It also states that in order to effectively reach these benefits, a “fundamental change in the philosophy of how structures are designed should occur”.

1.2. Membrane wings

In the history of airplane design, the use of thin, compliant membranes for the wing surfaces originates back to the beginnings of human flight. The wings of the "Wright Flyer" aircraft, the world's first successful powered airplane developed by the Wright Brothers flown in 1903, were made out of a thin membrane spanned over a rigid, load bearing structure ([3]). Later, as aircraft had to fly faster and carry more payload, much stronger structures were required to withstand the aerodynamic loads, discarding the use of membrane wings. However, the low weight, low cost and structural simplicity of membrane wings still continued to make of them an attractive technical solution for low speed applications. In the mid of the 20th century, membrane wings regain interest with the development of the so called Princeton sailwing (see Fig. 1). It basically consists of a rigid leading edge spar and a trailing edge wire spanned between a tip rib and a root rib with a flexible membrane wrapped around the leading and trailing edges, forming the upper and lower wing surfaces. In Refs. [4] and [5], experimental tests of different sailwing configurations show that their aerodynamic characteristics compare favourably with conventional rigid wings in terms of maximum lift and maximum lift-to-drag ratio. Moreover, a notable feature of sailwings is their ability to naturally adapt their shape to changing flow conditions, resulting in superior stall characteristics. More recently, membrane wings gained increased attention with the investigation of mammalian flight mechanics to understand how far their flexible wings are responsible for their outstanding flight capabilities ([9], [10]). Beside the pure biological interest, these investigations are also driven by the potential application of such wings for the design of micro sized air vehicles ([6], [7]).

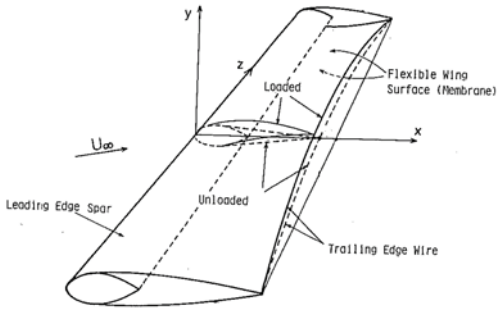

Fig. 1: Schematic of the Princeton sailwing ([8]).

1.3. The elastoflexible morphing wing

In this context, this paper considers the investigation of a wing concept that uses the high compliance, low weight and adaptability advantages of membrane wings as a technical solution for a morphing wing. The basic construction of this biologically inspired concept considered here is shown in Fig. 2. The load bearing structure consists of an articulating leading edge spar, with an elastic cover spanned over it to form the actual aerodynamic surface.

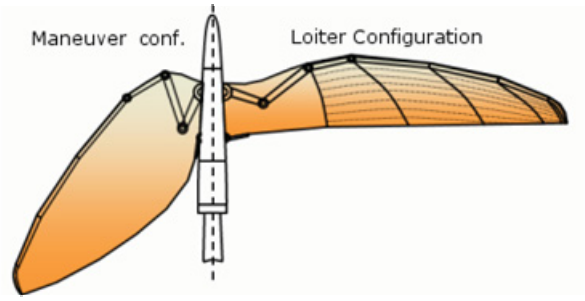

Fig. 2: Schematic of the elastoflexible morphing wing.

While the configuration of the actively controlled leading edge spar sets the overall planform of the wing, the highly extensible membrane used for the wing surface naturally adapts to the changing shape. Like this, a seamless aerodynamic surface can be obtained and the reconfiguration can be done with reasonable actuation energy. With this particular design, the wing planform can be continuously varied between a high aspect ratio, straight wing and a highly swept back, low aspect ratio configuration (referred to as the "loiter" and "maneuver" configurations, respectively). The investigation of this concept is carried out mainly experimentally by means of comprehensive tests of an appropriate wind tunnel model (see section 2.1). The flow structure interaction governing the behaviour of the wing is thereby rather complex since a variation of the configuration simultaneously affects the membrane characteristics (prestrain), and the aerodynamic load as a result of the changing aspect ratio and sweep angle (see Fig. 3).

2. EXPERIMENTAL WORK

2.1. Wind tunnel model

The wind tunnel model used for the experimental investigations is shown in Fig. 4. For the leading edge spar, an asymmetric cross section is used to provide smoother pressure distributions compared to a simpler rounded one ([8]). Linkages are introduced between the different segments of the leading edge spar to coordinate their movements and allow the actuation of the model with a single stepper motor. The trailing edge consists of a telescopic bar which length passively adapts to the current wing configuration. Tab. 1 gives a summary of the morphing capability of this model in terms of the aspect ratio, sweep angle (at mid chord), wing area, wing span and mean chord length.

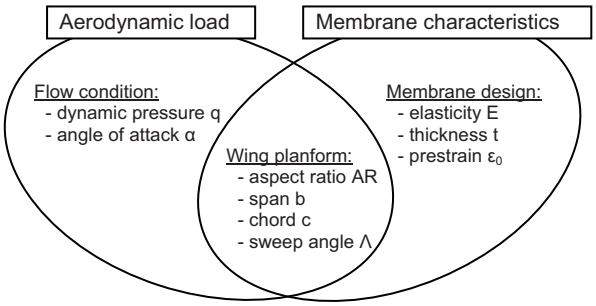

Fig. 3: Illustration of the coupled nature of the aeromechanics of the elastoflexible morphing wing.

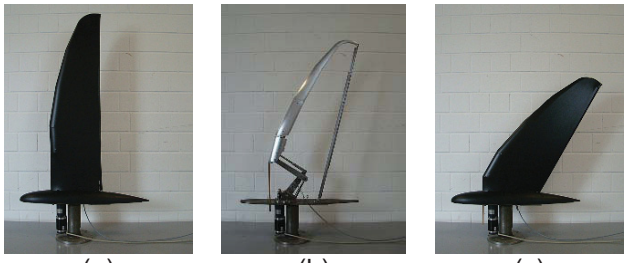

(a) (b) (c)

Fig. 4: Wind tunnel model. a) Loiter configuration, b) Articulating structure (intermediate configuration), c) Maneuver configuration.

	Loiter conf.	*Maneuver conf.*
Aspect Ratio AR [-]	8.6	4.6
Sweep angle $\Lambda_{1/2}$ [deg]	6	36
Half area S/2 [m^2]	0.23	0.2
Half span b/2 [m]	1	0.6
Mean chord c [m]	0.232	0.263

Tab. 1: Geometric characteristics of the morphing wind tunnel model.

The membrane currently used for the wing surface consists of an elastic fabric coated on one side with a rubber layer to ensure air impermeability. A suitable cut has been designed in order to avoid crinkles and provide some pretension in all configurations. Thereby, the pretension obviously depends on the configuration and to illustrate this, Fig. 5 shows the prestrain of the membrane in the loiter and maneuver configurations, measured on the lower side of the wing using a 2D photogrammetry technique. Here, the prestrains $\varepsilon_{0,chord}$ and $\varepsilon_{0,span}$ indicate the elongation of the grid lines in the chordwise and spanwise directions, respectively, relatively to the initial membrane cut. While the loiter configuration exhibits a much higher spanwise prestrain due to its larger span (up to 40%) and almost no chordwise prestrain, the maneuver configuration exhibits just the opposite pattern with a chordwise prestrain up to 15%.

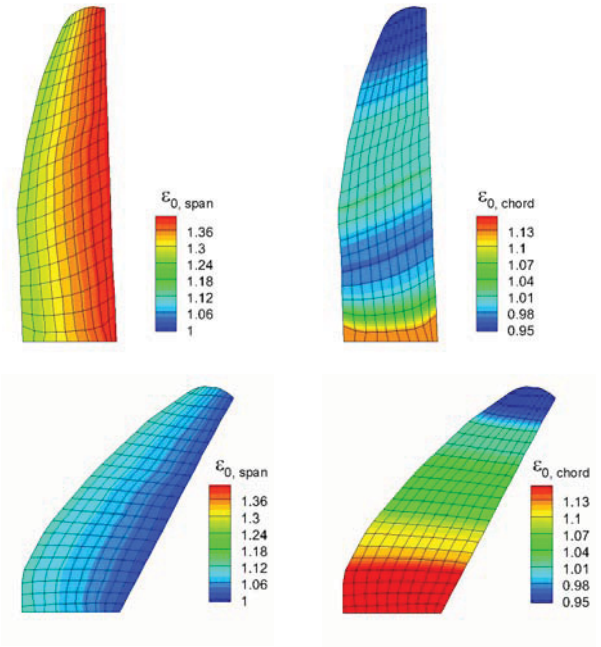

Fig. 5: Membrane prestrain.

2.2. Experimental setup

The morphing wing model presented above was tested in the low-speed wind tunnel facility “A" of the Institute of Aerodynamics and Fluid Mechanics of the TU München. It has an open rectangular test section of 1.8 m height by 2.4 m width and 4.8 m length and generates wind speeds up to 65 m/s with a freestream turbulence level below 0.4%.

2.2.1. Force measurements

For the measurements of the lift and drag characteristics, the wing model was fixed on an external 6-components aerodynamic balance placed under the floor of the test section, allowing recording time averaged forces. In order to avoid interactions of the model with the boundary layer developing on the floor of the test section, the model is elevated by around 140 mm above the ground using a peniche. The lift and drag characteristics were measured for five different wing configurations including the loiter and maneuver configurations shown in Fig. 4 as well as three intermediate configurations. Three different flow conditions were investigated, namely dynamic pressures of q = 135 Pa, q = 310 Pa and q = 535 Pa corresponding to freestream velocities of U_∞ = 15 m/s, U_∞ =22.5 m/s and U_∞ = 30 m/s, respectively, and Reynolds numbers of Re_c = $0.25 \cdot 10^6$, Re_c = $0.375 \cdot 10^6$ and Re_c = $0.5 \cdot 10^6$, respectively. The range of angles of attack investigated goes from α = -20° to α = +40° in one degree step. The forces were measured during both the increasing (from -20° to +40°) and the decreasing (from +40 to -20°) angle of attack phase. Finally, at each angle of attack, time averaged forces over 30 seconds were recorded.

2.2.2. Deflection measurements

The setup for the deflection measurements is shown in Fig. 6. The stereo photogrammetry system used is composed of two *FlowSense 2M* cameras placed outside of the wind tunnel test section with approximately 40° angle of separation between their respective optical axes. The cameras have a resolution of 1600 x 1186 pixels which, in conjunction with the imaging optics (*Nikon*, focal length 135 mm, aperture 1:28) and the distance to the model, provides an average spatial resolution of 0.15 mm per pixel. A self developed software using the Direct Linear Transformation method (*DLT*, [14]) was used to recover the 3D coordinates of each of the 230 markers put on the upper and lower wing surfaces, respectively (23 markers in spanwise and 10 in chordwise direction, consisting of white stickers of 5 mm diameter). A calibration target consisting of a 2D grid of markers defining the x-y plane and moved to several z-positions is used to obtain the transformation parameters necessary to reconstruct the coordinates in the object space with *DLT*. The reconstruction of the calibration points in the object space from the calibration images using the transformation parameters obtained indicates an average measurement uncertainty of 0.085 mm within the control volume. Due to the small size of the control volume imposed by the imaging optics, the measurement of a complete wing consists of 11 separate measurements patched together. For this, a traversing unit was used to move the measurement volume into the desired positions along the wing. However, the travelling length of the traversing systems available was not sufficient to measure the complete wing. For this reason, results at the wing root of both configurations and at wing tip of the upper side of the loiter configuration are not available. The deflection measurements so far were performed only on the loiter and maneuver configurations, at freestream dynamic pressure of q = 135 Pa and q = 535 Pa, and for angles of attack of of α = 0°, 5°, 10°, 15° and 20°.[1]

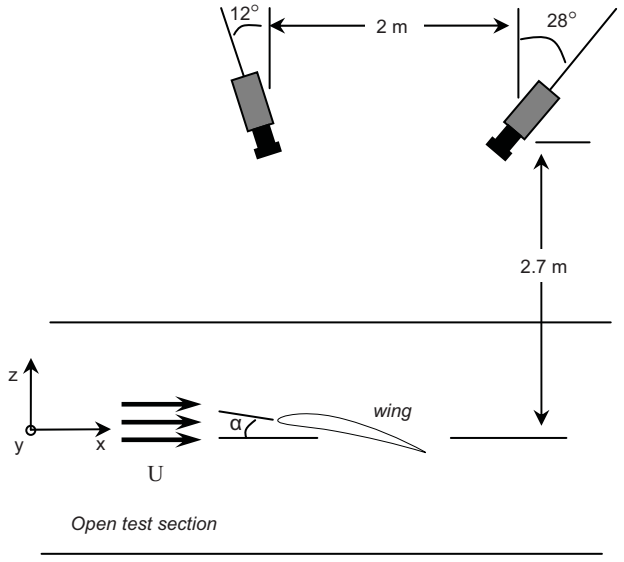

(a)

[1]Only instantaneous measurements were performed. For the maneuver configuration, the results at α = 20° and q = 535 Pa could not be properly analyzed because of strong vibrations of the membrane.

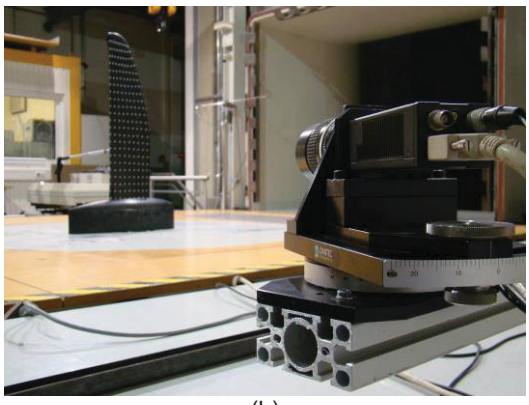

(b)

Fig. 6: (a) Schematic showing the experimental setup for the deflection measurements. (b) Real setup.

3. RESULTS AND DISCUSSION

3.1. Lift and drag characteristics

Fig. 7 shows the measured lift curves of the loiter and maneuver configurations[2]. The dynamic pressure dependency is clearly visible, namely the lift curves become steeper with increasing aerodynamic loading as a result of the large membrane deflection. At q = 135 Pa, the lift characteristics are largely linear indicating that the wing behaves more like a rigid wing, accordingly to the rather limited membrane deflection at this flow condition. In contrast, the lift curves at q = 535 Pa become non-linear as a result of the massive deformation induced by the high aerodynamic load. The stall characteristics are also strongly affected by the level of dynamic pressure. In fact, the curves at q = 535 Pa highlight an overall delayed stall and reach higher maximum lift coefficients. The maneuver configuration (Fig. 7b) shows a more regular behaviour with a less pronounced dependency on the dynamic pressure, which is explained by the higher chordwise prestrain associated with this configuration (cf. Fig. 5). The drag polars shown in Fig. 8 highlight a pronounced dependency on the dynamic pressure, too. Interestingly, for both configurations, the shape of the drag polar indicates an improved efficiency as the aerodynamic loading increases, with lower minimum drag and lower lift-induced drag. The diagrams of Fig. 9 showing the corresponding lift-to-drag ratios confirm this. The loiter configuration highlight optimal performances at q = 310 Pa. For the maneuver configuration, the best aerodynamic efficiency is reached at the highest aerodynamic loading. In this case, a further increase of the dynamic pressure may lead to still improved aerodynamics until an optimum is reached. This point emphasizes the sensitivity of the aerodynamic performances to the flow condition, and indicates that the passive deformation of the membrane may lead to an optimal wing geometry at some given aerodynamic loading, or, regarding further concept stages, that a specific membrane design can be used to optimize the performances of the wing.

[2] For clarity, only averaged forces between the increasing and decreasing angle of attack strokes are considered here.

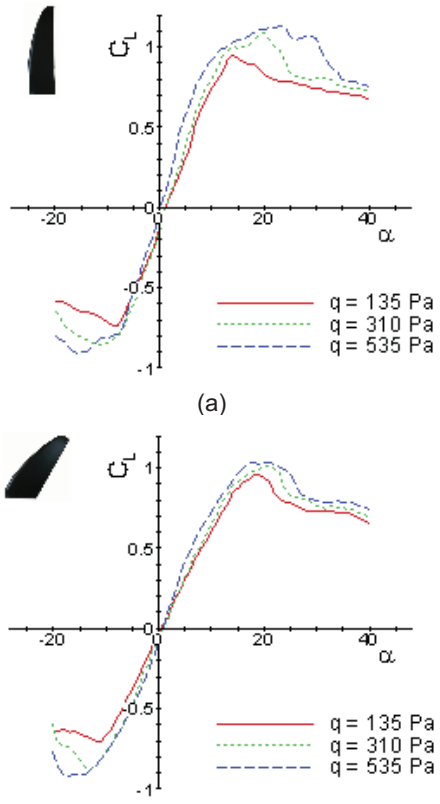

(a)

(b)

Fig. 7: Lift characteristics of the loiter (a) and maneuver (b) configurations.

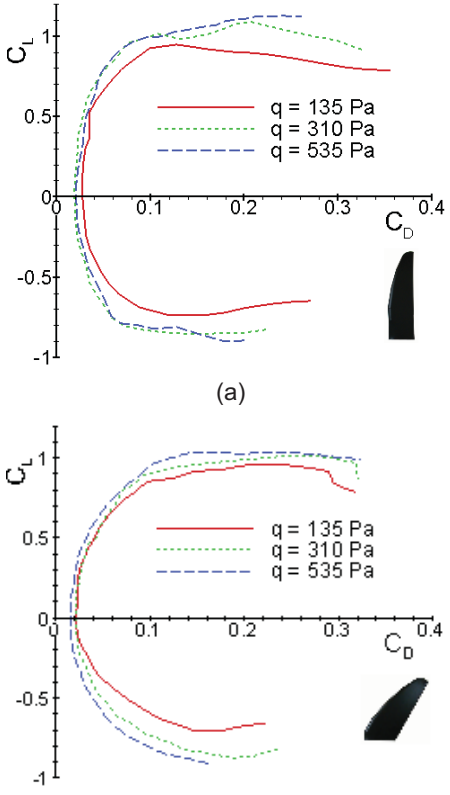

(a)

(b)

Fig. 8: Drag characteristics of the loiter (a) and maneuver (b) configurations.

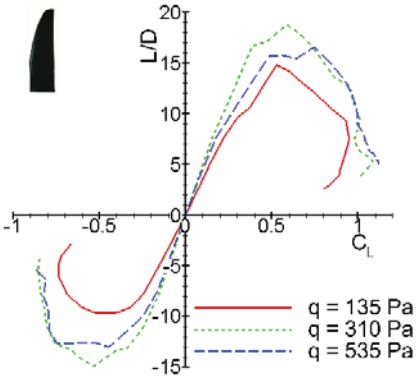

(a)

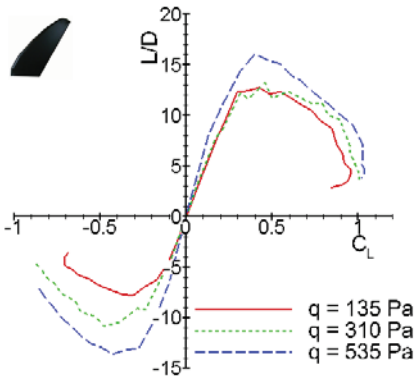

(b)

Fig. 9: Lift-to-drag ratio of the loiter (a) and maneuver (b) configurations.

In the following, a comparison of the lift and drag characteristics of the five configurations investigated is presented in order to assess the effectiveness of the planform morphing to alter the aerodynamic characteristics. The comparison is based on the lift curve slope $C_{L,\alpha}$, the minimum drag coefficient C_{Dmin}, the lift-induced drag factor K and the maximum lift to drag ratio $(L/D)_{max}$. Thereby, $(L/D)_{max}$ is directly taken from the experimental data whereas the remaining parameters are obtained by fitting the linear lift and quadratic drag polar models from the rigid wing theory to the measured data (see Eqs. (1) and (2)). Even if the experimental data show some decided discrepancies from conventional rigid wings, especially at high aerodynamic loading, this approach allows to capture the main trends. For the model fit, only the experimental data measured between α = -5° and α = 10° are taken into account to filter out the non-linearities due to flow separation and effectively capture the influence of the wing planform and elasticity.

(1) $$C_L(\alpha) = C_{L0} + C_{L\alpha}\alpha$$

(2) $$C_D(C_L) = C_{D\min} + K(C_L - C_{L0})^2$$

The surface plots given in Fig. 10 (a) through (d) show the variation of $C_{L,\alpha}$, C_{Dmin}, K and $(L/D)_{max}$, respectively, as a function of the wing configuration (represented here by the aspect ratio, AR) and of the aerodynamic loading (dynamic pressure, q). At any flow condition, the lift curve slope $C_{L,\alpha}$ (Fig. 10a) is found to decrease as the aspect ratio reduces, which is consistent with the known trends from rigid wing theory. Beside this, increasing the dynamic pressure leads to higher values of $C_{L,\alpha}$ for all configurations, accordingly to the observations made in Fig. 7. The minimum drag C_{Dmin} in Fig. 10b is found to globally decrease with decreasing aspect ratio, because the associated variation in span and sweep angle reduces the wetted area of the wing. Further, C_{Dmin} globally decreases as the aerodynamic loading increases, which is explained by the associated variation of the Reynolds number on the one hand, and by the difference in profile drag associated with the current deformed wing geometry on the other hand. The lift-induced drag factor K (Fig. 10c) is found to decrease with increasing aerodynamic loading. The way C_{Dmin} and K vary with the aerodynamic loading is consistent with the drag polar shapes observed in Fig. 8. Moreover, the variation of C_{Dmin} and K with the planform indicate that low aspect ratio configurations are advantageous for high speed flight because they feature less drag at low lift coefficients, whereas the high aspect ratio configurations features just the opposite with a lower drag at higher lift coefficients, thus being more efficient for low speed flight. Known from the rigid wing theory, these trends also apply in the case of the elasto-flexible morphing wing considered here. Finally, Fig. 10d shows the maximum lift-to-drag ratios corresponding to each tested case. In the case of the loiter configuration, $(L/D)_{max}$ reaches a global maximum at q = 310 Pa as already observed in Fig. 9a, whereas all other configurations show monotonic increase of their respective $(L/D)_{max}$ with the aerodynamic loading. This is explained by the difference in membrane characteristics where the low chordwise prestrain of the loiter configuration allows “too much” deformations, thus deteriorating the performances. In the other cases, a further increase of the dynamic pressure may lead to even higher lift-to-drag ratios until an optimum is reached. Beside this, $(L/D)_{max}$ globally drops with decreasing aspect ratio as expected from rigid wing theory.

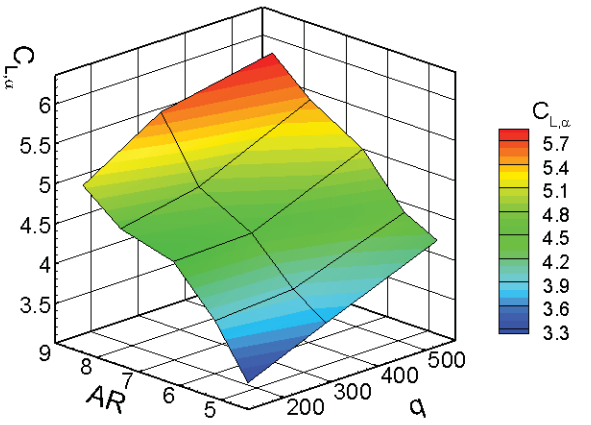

(a) Lift curve slope $C_{L,\alpha}$

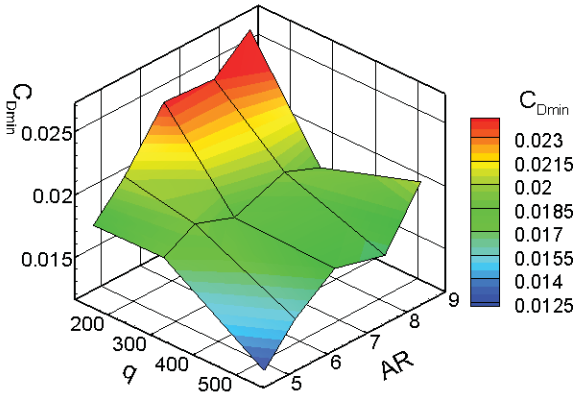

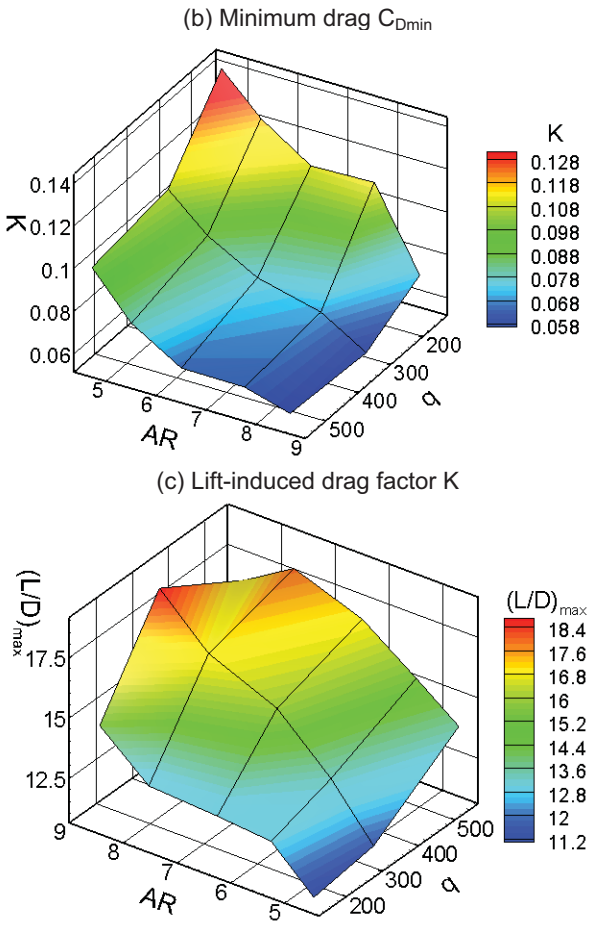

Fig. 10: Synthesis of the aerodynamic characteristics of the morphing wing.

To summarize, the wing globally features better performances at higher aerodynamic loading with increased lift production and higher lift-to-drag ratios. The results of the deflection measurements presented in the following section will provide quantitative information about the actual deformed wing shapes and help to understand the specific features observed here.

3.2. Membrane deformation

To analyse the overall deformation pattern of the aerodynamically loaded membrane, Fig. 11 shows the normalized deflection relatively to the unloaded wing, Δz/c, of the upper and lower sides at q = 535 Pa and α = 5° (similar deformation patterns were observed at the other flow conditions investigated). On the upper side, the accelerating airflow creates a suction force that deflects the membranes upward. On the lower side, the pressure rises and deflects the membrane upwards, too, but with lower amplitude. As a result, the deflection of the membrane directly influences the camber distribution of the wing. Both the loiter and the maneuver configurations exhibit a maximum deflection in the central part of the wing with a zero deflection at the leading and trailing edge as well as at the wing root and wing tip since the membrane is constrained there.

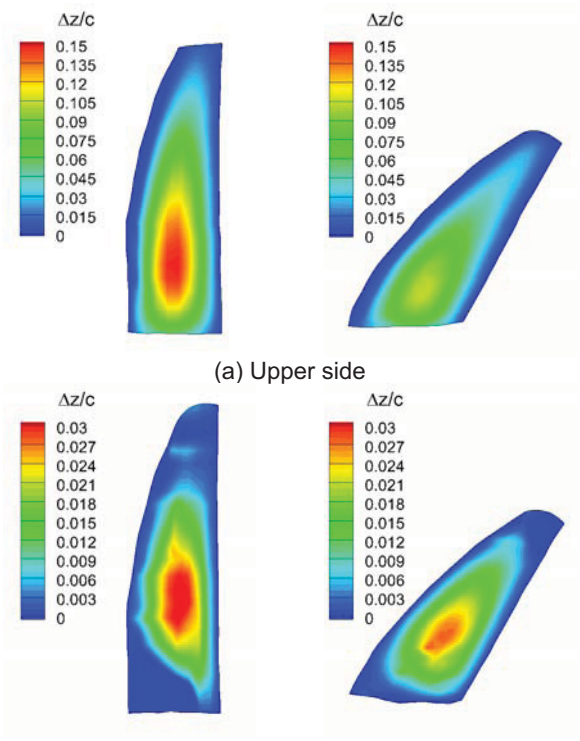

Fig. 11: Membrane deflection at q = 535 Pa and α = 5°.

Fig. 12 and Fig. 13 show the distribution of the local maximum deflection, $\Delta z_{max}/c$, along the span of the upper side of the loiter and maneuver configurations as a function of the angle of attack for both dynamic pressures investigated. In all cases, similar shapes of the distribution are found with a "zero" deflection at the root and at the tip because the membrane is fixed on the structure there, and a maximum deflection around 2y/b = 0.3. The different deflection amplitudes between the cases at q = 135 Pa and q = 535 Pa emphasizes the strong dependency of the wing geometry (i.e., camber distribution) on the flow conditions, which is responsible for the spread in aerodynamic characteristics observed in the previous section. Thereby, the deflection amplitude does not exactly scale with the dynamic pressure, which indicates the non-linearity of the flow-structure interaction. The amplitude of the deflection in the case of the maneuver configuration at equivalent flow conditions is overall lower than in the case of the loiter configuration, which is the result of tow different influences. On the one hand, the reduced aspect ratio of this configuration mitigates the aerodynamic load, and on the other hand, its higher chordwise prestrain (see Fig. 5) limits the deflection. This emphasizes the coupled nature of the flow-structure interaction mechanisms involved here, namely that the planform variation influences simultaneously the aerodynamic load and the membrane characteristics, making it difficult to clearly assess the relative contribution of each effect. Further, the fact that the deflection of the maneuver configuration is less even if it has a much lower spanwise prestrain indicates that the chordwise prestrain has a bigger impact on the deflection than the spanwise prestrain.

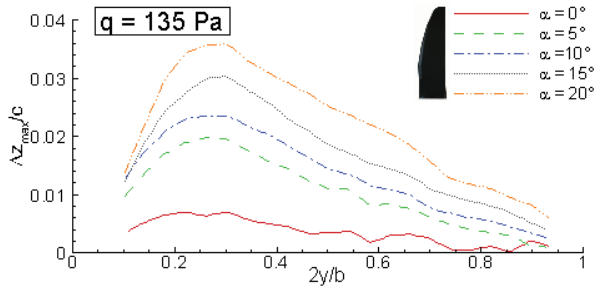

(a)

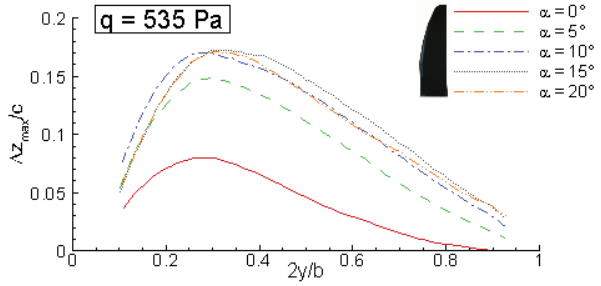

(b)

Fig. 12: Spanwise distribution of the maximum deflection, loiter configuration.

Coming back to Fig. 12 and Fig. 13, in general, the deflection grows roughly monotonically with the angle of attack except in Fig. 12b where it stays constant after α = 10°. Interestingly, the slope of the corresponding lift curve in Fig. 7a becomes significantly lower after α = 10° indicating the onset of stall. The flow separation induced by the massive camber limits the aerodynamic load on the membrane and discards a further increase of the deflection accordingly. Finally, in all cases except the one in Fig. 13a, the deflection grows more rapidly between α = 0° and α = 5° than for higher angles of attack. This so called hysteresis effect occurs because the situation around α = 0° is unstable since the direction of the aerodynamic load is not clearly defined (i.e., zero lift). At higher angles of attack, however, the direction is uniquely defined and the membrane "snaps" to a stable shape. This effect is known to be strongly influenced by the chordwise prestrain of the membrane, which is also verified here since it is more pronounced in the case of the loiter configuration where the chordwise prestrain is much lower than for the maneuver configuration (cf. Fig. 5). Here again, the chordwise prestrain seems to play a more important role than the spanwise prestrain.

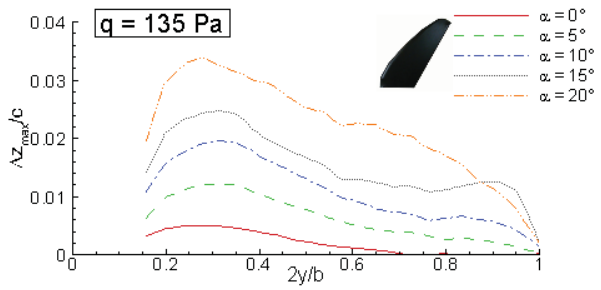

(a)

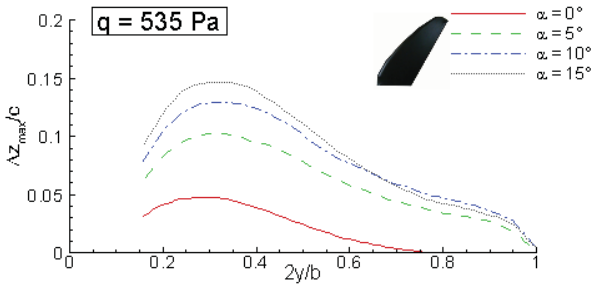

(b)

Fig. 13: Spanwise distribution of the maximum deflection, maneuver configuration.

3.3. Airfoil sections

The deflection measurements of the upper and lower sides can be put together to analyse the airfoil shapes constituting the wing at the different flow conditions. Fig. 14 shows the airfoil shapes of the loiter configuration occurring at α = 0°, 5° and 10°, for q = 135 Pa and q = 535 Pa, respectively, taken at 2y/b = 0.3 (approximate location where the maximum deflection occurs). At the lowest aerodynamic loading, q = 135 Pa, the deflection is rather limited and the camber just slightly grows with the angle of attack, as a result of the increasing suction force on the upper side and rising pressure force on the lower side. The same section look totally different at q = 535 Pa. The high aerodynamic loading induces massive deflections resulting in radically different airfoil shapes compared to the case at q = 135 Pa. At α = 0°, the symmetrical flow condition results in a suction force on both the upper and lower wing surfaces, explaining the drop-like airfoil shape. However, this is an unstable situation since the direction of the load is not clearly defined (i.e., zero lift) and, as the angle of attack increases, the membrane “snaps” into a more stable shape with a positive camber. After this abrupt shape change has occurred, the camber grows with the angle of attack and sees its maximum moving towards the leading edge at the same time, due to the increasing suction load at the leading edge. This pronounced angle of attack dependency of the camber at q = 535 Pa explains the higher lift level and the steeper slope of the lift curve observed in section 3.1. In Fig. 14b, the global upward shifting of the airfoils indicates that the articulating structure of the wing bends under the high aerodynamic load. Thereby, the bending is higher at the trailing than at the leading edge, resulting in a slight decrease of the effective angle of attack (approximately -2.5° between α = 0° and α = 10°).

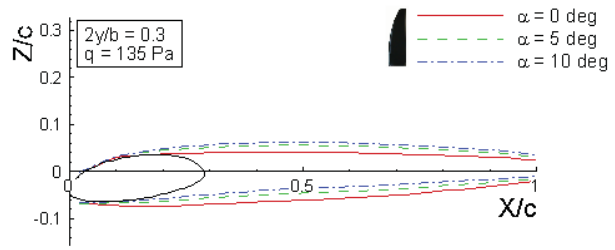

(a)

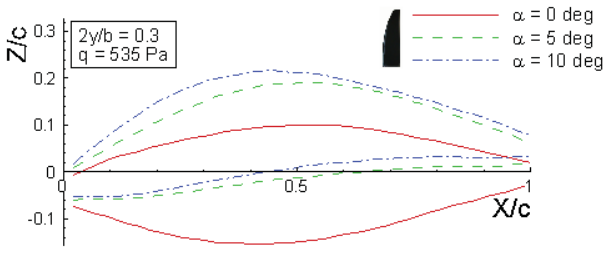

(b)

Fig. 14: Airfoil sections at 2y/b = 0.3, loiter configuration. (a) q = 135 Pa, (b) q = 535 Pa. The geometry of the leading edge spar is schematically represented in diagram (a).

Fig. 15 shows the corresponding airfoil shapes of the maneuver configuration, also taken at 2y/b = 0.3. In general, the same comments than those concerning the loiter configuration can be made here, except that the amplitude of the deflection is overall less in this case because of the lower aerodynamic load and the higher chordwise prestrain associated with this planform. This is also in accordance with the observations made in section 3.1, where the dynamic pressure dependency of the lift and drag characteristics was found to be less pronounced for this wing configuration than for the loiter one. In Fig. 15b, almost no upward bending of the wing structure is observed here compared to Fig. 14b, because the structure is much stiffer in this configuration (lower span and fully retracted trailing edge).

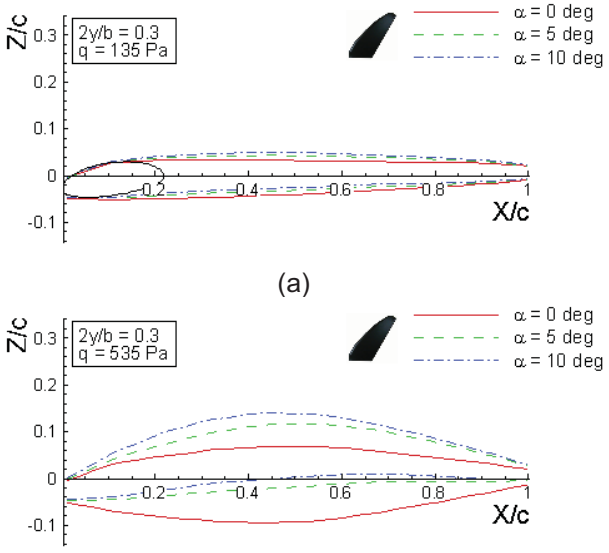

(a)

(b)

Fig. 15: Airfoil sections at 2y/b = 0.3 of the maneuver configuration. (a) q = 135 Pa, (b) q = 535 Pa The geometry of the leading edge spar is schematically represented in diagram (a).

In order to analyse the principal characteristics of the pressure distribution around airfoils corresponding to those shown in Fig. 14 and Fig. 15, the software *Xfoil* has been used to compute two different airfoils showing similar characteristics in camber and leading edge spar geometry to those experimentally observed. In the following, both airfoils are referred to as the "lowly loaded" and "highly loaded" airfoils, corresponding to the flow conditions at q = 135 Pa and q = 535 Pa, respectively. Fig. 16 show as example the pressure distributions computed for α = 5°. In the more conventional "lowly loaded" case, the pressure distribution on the upper side highlights a pressure minimum (suction peak) at the leading edge, followed by a monotonic pressure increase towards the trailing edge. In contrast, the pressure distribution on the upper side of the "highly loaded" airfoil looks totally different. The suction peak, somehow weaker than in the "lowly loaded" case, due to the larger camber, is followed by a local pressure recovery, before the pressure decreases again to finally reach a global pressure minimum around X/c = 0.5. After this, the pressure recovery towards the trailing edge occurs with a much steeper adverse pressure gradient than for the "lowly loaded" airfoil.

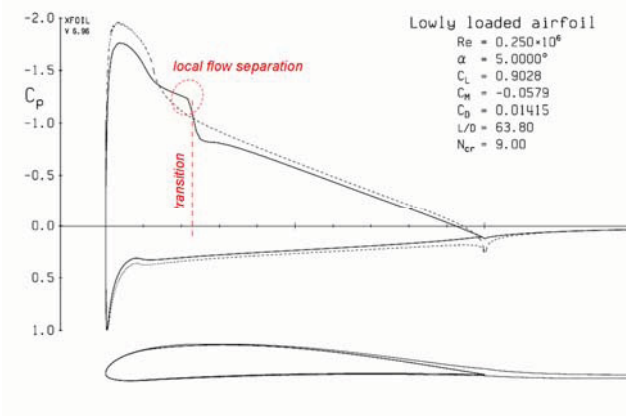

(a)

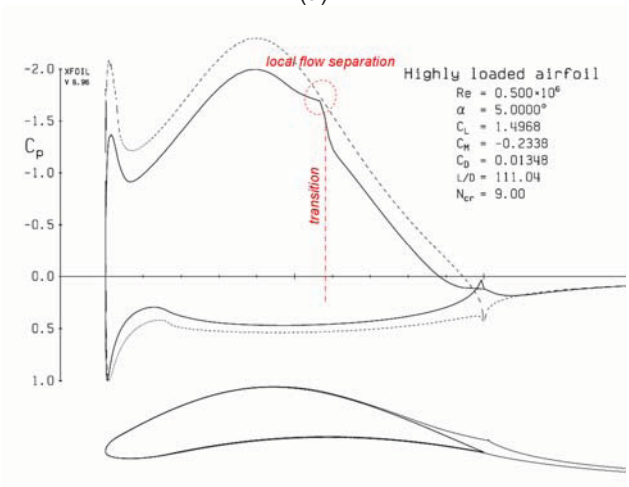

(b)

Fig. 16: Pressure distributions at α = 5° (*Xfoil* results).

In both cases, the pressure distribution on the upper side in the viscous case show a local plateau indicating the presence of a laminar separation bubble, after which the boundary layer becomes turbulent. *Xfoil* predicts a much longer laminar flow portion in the case of the "highly loaded" airfoil than in the "lowly loaded" case, with a transition at x/c ~ 0.57 and x/c ~ 0.22, respectively. Additional computations with these airfoils showed that, at equivalent lift coefficient, the "highly loaded" case features a much lower profile drag (about 30% less) than the "lowly loaded" geometry. These results are consistent with the experimental observations made in section 3.1 where the minimum drag was observed to be reduced at higher aerodynamic loading.

4. CONCLUSION AND OUTLOOK

This paper considered the experimental investigation of an elasto-flexible morphing wing concept using a compliant membrane as aerodynamic surface to allow large variations of the planform. Results of force measurements together with quantitative measurements of the membrane deflection were presented to assess the performances and the aero-elastic behaviour of the wing. The results of the force measurements showed that morphing the planform geometry can be effectively used to adapt the lift and drag characteristics of the wing to varying flow conditions. Thereby, the basic influence of the planform geometry is found to be consistent with the trends expected from rigid wing theory. The lift and drag characteristics highlight also a pronounced dependency on the aerodynamic loading, because the highly elastic wing surface passively deflects under aerodynamic loading. The results of the deflection measurements indicate the broad range of shapes the airfoils can take depending on the flow conditions. Thereby, the dynamic pressure is found to have a strong influence on the overall camber line, thus lift level, whereas the angle of attack affects the airfoil shape more subtly by inducing smaller changes in the position and amplitude of the maximum camber. Beside this, the wing planform was found to have a significant influence on the deflection, too, because it simultaneously affects the prestrain of the membrane and the aerodynamic load as a result of the variation in aspect ratio and sweep angle. Consequently, the maneuver configuration show overall lower deflection amplitudes with less cambered airfoils than the loiter configuration at equivalent flow conditions. This point indicates that an active control of the chordwise prestrain, for example by varying the position of the trailing edge spar, could be used to adjust the camber at any flow condition. Like this, the high compliance of the wing surface could be taken advantage of not only to allow for large variations of the planform, but rather to adjust all the main aerodynamically relevant geometrical parameters of the wing. The future development and investigations of the concept will concentrate on this aspect. Experimental tests with an extended wind tunnel model as well as numerical simulations for optimization purposes are planned.

5. REFERENCES

[1] Rodriguez A. R.: *Morphing Aircraft Technology Survey*. AIAA-2007-1258, 45th AIAA Aerospace Sciences Meeting and Exhibit, 2007.

[2] Thill, C., Etches, J.: *Morphing Skins*. The Aeronautical Journal, paper No. 3216, 2008.

[3] Anderson, J.D.: *Aircraft Performances and Design*. McGraw-Hill International Editions, 1996.

[4] Fink, M. P.: *Full-scale Investigation of the Aerodynamic Characteristics of a Sailwing of Aspect Ratio 5.9.* Technical Note D-5047, NASA Langley Research Center, 1969.

[5] Maughmer, M.D.: *A Comparison of the Aerodynamic Characteristics of Eight Sailwing Airfoil Sections.* Technical Report, Princeton University, 1979.

[6] Yongsheng, L., Shyy, W.: *Laminar-Turbulent Transition of a Low Reynolds Number Rigid and Flexible Airfoil.* AIAA Journal, Vol. 45, No. 7, 2007, pp.1501-1513.

[7] Hu, H., Tamai, M.: *Flexible-Membrane Airfoils at Low Reynolds Number.* Journal of Aircraft, Vol. 45, No. 5, 2008, pp. 1767-1778.

[8] Murai, H., Maruyama, S.: *Theoretical Investigation of Sailwing Airfoils Taking Account of Elasticities*, Journal of Aircraft, Vol. 19, No.5, 1982, pp. 385-389.

[9] Song, A. J., Tian, X.: *Aeromechanics of Membrane Wings with Implications for Animal Flight*. AIAA Journal, Vol. 46, No. 8, 2008, pp. 2096-2106.

[10] Waldmann, R.M., Song, A. J.: *Aerodynamic Behaviour of Compliant Membranes as Related to Bat Flight*. AIAA-2008-3716, 38th Fluid Dynamics Conference and Exhibit, 2008.

[11] Abdulrahim, H., Lind, R.: *Using Avian Morphology to Enhance Aircraft Manoeuvrability*. AIAA-2006-6643, AIAA Athmospheric Flight Mechanics Conference and Exhibit, 2006.

[12] Moorhouse, D., Sanders, B.: *Benefits and Design Challenges of Adaptive Structures for Morphing Aircrafts*. The Aeronautical Journal, paper No. 3012, 2006.

[13] Eschler Textil GmbH. *http://www.eschler.com*.

[14] Luhmann, T.: *Close Range Photogrammetry*. Wiley, 2nd edition, 2006.